ATR-FTIR and XRD quantification of solid mixtures using the asymptotic constant ratio (ACR) methods. Application to geological samples of sodium and potassium feldspars

Antonio Doménech-Carbó*, Francisco Bosch-Reig, Noemí Montoya

Departament de Química Analítica, Universitat de València, Dr. Moliner 50, 46100 Burjassot, Valencia, Spain.

* Corresponding author: e-mail: antonio.domenech@uv.es.

Abstract

Two asymptotic constant ratio methods applied to the quantification of individual components of solid samples using attenuated total reflectance-Fourier transform infrared spectroscopy (ATR-FTIR) and X-ray diffraction (XRD) are described. The methods involve the measurement of the peak current/peak areas of selected signals (diffraction peaks in XRD and absorption bands in ATR-FTIR) relative to the signal of standard added in constant proportion to the sample and the sample enriched with the analyte following the usual standard additions methodology. The proposed method compensates the absorption effects appearing in XRD and the presence of overlapping absorption bands of interferents by means of an asymptotic representation thus avoiding the need of the knowledge of the absorption parameters of the matrix and analytes. The method was tested for mixtures of different metal oxides and sodium and potassium feldspars with satisfactory results.

Keywords: XRD; ATR-FTIR; Quantification; Constant ratio asymptotic; Feldspars.

1. Introduction

The identification and quantification of individual components in mixtures is of interest in several fields, including in particular mineral analysis, where attenuated total reflectance-Fourier transform infrared spectroscopy (ATR-FTIR) and X-ray diffraction (XRD) techniques are frequently combined [1-4]. Apart from the obvious application to mineral ores [5], this kind of studies deals with dust aerosols [6-9], soils [10-12], meteorites [13], and historical monuments [14], among others.

One general problem to be faced is the determination of the concentration of an individual species in a solid mixture of unknown composition. In the case of XRD, the main difficulty for this purpose is that the peak currents and/or peak area measurements are conditioned by absorption effects, thus making inapplicable usual methods of quantification used in spectroscopies [15,16]. Then, different methods of XRD data treatment have been proposed, namely, reference intensity ratio (RIR), mineral intensity factor (MIF), multiphase Rietveld refinement, and full pattern summation [17,18]. The matrix flushing method or the normalized RIR (Reference Intensity Ratio) [19-21] performs a least squares fitting of the full experimental pattern to the identified phases in the mixture. Historically, these methods and full-pattern fitting methods [22,23] have been considerably developed, ideally requiring the knowledge of the diffraction pattern of individual components of the sample as well as their mass absorption coefficients, as demanded by the Klug's equation [24]. The need of the knowledge of such individual mass absorption coefficients and the presence of amorphous materials and high crystallographic complexity made difficult, however, the quantification by XRD, as recently reviewed [17,18].

In the case of ATR-FTIR, there are two general difficulties for quantification purposes: the presence of components in the sample whose spectrum overlaps with the spectrum of the analyte and the variability of the optical path in turn depending on the composition of the whole sample, thus hindering the application of classical quantification methods of application in uv-vis spectroscopy [25-27].

In previous works, methods yielding the absolute concentration of an analyte in a solid sample containing N absorbing substances with non-overlapping [28] and overlapping

[29] bands were described. These methods were based on the addition of an internal standard in constant concentration (constant-ratio methodology) accompanying standard additions of the analyte and required the validity of the Beer-Lambert law and the equality of the optical paths for a given spectrum at all wavenumbers.

The purpose of the current work is to present two constant-ratio analytical methods specifically and respectively applied to ATR-FTIR and XRD quantification extending the philosophy of the constant ratio methods compensating the optical path effect in ATR-FTIR and the absorption effects in XRD for samples of unknown composition. In both cases, the experimental procedure involves the addition of an internal standard in fixed proportion and the subsequent performance of standard additions of the analyte. The treatment in the case of XRD is based on the Klug's equation and the effect of the absorption of the unknown matrix is compensated by means of an asymptotic representation. In the case of ATR-FTIR, the asymptotic representation permits to compensate the influence of the variable, matrix-dependent optical path.

The resulting asymptotic constant ratio XRD-ACR and ATR-ACR methods have been tested by the quantification of individual crystalline solids in mixtures of sodium and potassium feldspars. These are of particular interest because of its application in ceramics [30] and environmental [31], mineralogical [32,33] and archaeological [34-38] significance. In the case of XRD TiO_2 (anatase) was used as the internal standard because of its good crystallinity, high purity, chemical inertness and well-defined XRD response and a previous test using mixtures of pure reagents, Cr_2O_3 and NiO, was carried out. In the case of ATR-FTIR, $KHCO_3$ was used as the internal standard. This compound shows both overlapping and non-overlapping bands with those of the feldspars, thus illustrating the application of the method to the most unfavorable case of some interference of the internal standard.

2. Experimental

Anatase (TiO_2, Carlo Erba), $KHCO_3$, NiO, and Cr_2O_3 (all Probus reagents) were used. Mixtures of analyte/standard were prepared in different proportions, weighing each component on an analytical balance to obtain different binary, ternary, etc. mixtures. The standards were: sodium feldspar (LGC Standards, BCS-CRM Nº 375/1), potassium

feldspar (NCS DC 61102, China National Analysis Center for Iron and Steel), quartz (high purity silica, BCS-CRM 313/2) and kaolin (NCS DC 60123a, China National Analysis Center for Iron and Steel). The certified composition of such standards is summarized in Table 1. For obtaining the diffractograms of reference minerals, an amount of 0.200 g of the mineral was finely powdered with an agate mortar and pestle and passed through a 500 μm sieve.

XRD analysis of powder samples (Model D-8 Advance, Bruker) was performed using CuKα radiation. The diffractometer had two 1 mm divergence slit, the scatter and receiving slits being 3 mm and 3º, respectively. The X-ray powder diffraction patterns were run with a step size of 0.02 2θº and a counting time of 0.2 s. The determination of the lattice constants of zircon was made using the Rietveld indexing program.

ATR-FTIR spectra were recorded with a Vertex 70 Fourier transform infrared spectrometer with an FR-DTGS (fast recovery deuterated triglycine sulphate) temperature-stabilized coated detector. The spectra were recorded in the wavenumber region between 600 and 4000 cm^{-1} taken 32 co-added scans with a resolution of 4 cm^{-1}.

3. Description of the methods

3.1. XRD-ACR method

In the most simple case, we can consider a solid sample containing a binary mixture of two crystalline components, X, Y. Assuming that the diffractograms of X and Y are known and that do not contain overlapping peaks, we can express the mass fraction f_Y of the component Y as a function of the intensity (or area) of a given peak characteristic of Y recorded in the diffractograms of the pure component, I_Y^0, and the sample, I_Y, by means of the Klug's equation. This implies that the mass absorption coefficients of X and Y, B_X, B_Y, are known:

$$f_Y = \frac{(I_Y / I_Y^o) B_Y}{B_Y - (I_Y / I_Y^o)(B_Y - B_X)} \qquad (1)$$

Rearranging terms in the above equation yields:

$$I_{\mathrm{Y}} = I_{\mathrm{Y}}^{\mathrm{o}} \frac{f_{\mathrm{Y}} B_{\mathrm{Y}}}{B_{\mathrm{Y}} + f_{\mathrm{Y}}(B_{\mathrm{Y}} - B_{\mathrm{X}})} = I_{\mathrm{Y}}^{\mathrm{o}} \frac{f_{\mathrm{Y}}}{1 + f_{\mathrm{Y}}(1 - b_{\mathrm{XY}})} \qquad (2)$$

where $b_{\mathrm{XY}} = B_{\mathrm{X}}/B_{\mathrm{Y}}$.

Now, consider a standard additions experiment in which samples enriched in the component Y with added mass fractions f_{Y}^{*} are processed. The intensity of the selected Y- characteristic diffraction peak, I_{Y}^{*}, verifies:

$$I_{\mathrm{Y}}^{*} = I_{\mathrm{Y}}^{\mathrm{o}} \frac{f_{\mathrm{Y}} + f_{\mathrm{Y}}^{*}}{1 + (f_{\mathrm{Y}} + f_{\mathrm{Y}}^{*})(1 - b_{\mathrm{XY}})} \qquad (3)$$

Eliminating the term $1-b_{\mathrm{XY}}$ between equations (2) and (3) gives:

$$(1 - b_{\mathrm{XY}}) = \frac{I_{\mathrm{Y}}^{\mathrm{o}} f_{\mathrm{Y}} - I_{\mathrm{Y}}}{f_{\mathrm{Y}}} = \frac{(f_{\mathrm{Y}} + f_{\mathrm{Y}}^{*}) I_{\mathrm{Y}}^{\mathrm{o}} - I_{\mathrm{Y}}^{*}}{f_{\mathrm{Y}} + f_{\mathrm{Y}}^{*}} \qquad (4)$$

and:

$$I_{\mathrm{Y}}^{*} = I_{\mathrm{Y}} + \frac{I_{\mathrm{Y}}}{f_{\mathrm{Y}}} f_{\mathrm{Y}}^{*} \qquad (5)$$

This equation predicts that the representation of I_{Y}^{*} vs. f_{Y}^{*} corresponds to a straight line of ordinate at the origin I_{Y} and slope $I_{\mathrm{Y}}/f_{\mathrm{Y}}$, enabling for the determination of the mass fraction of the component Y in the sample, f_{Y}.

This treatment to a *N*-component sample is made difficult, even if amorphization effects are negligible, by the fact that the absorption contribution depends of all components. In this context, the above treatment can, in principle, be generalized to a mixture of crystalline compounds introducing mass absorption parameters b_{J} for each signal J which are function of the absorption coefficients of all components, in substitution of the two-component absorption ratio, b_{XY}.

For quantification purposes, we select a crystalline internal standard P, whose diffraction peaks do not overlap with those of the analyte Y. Then, we can prepare two binary mixtures, the first one containing the Y standard and an internal standard, P, and the second containing a mixture of the Y-containing sample enriched with P (the P-containing sample) so that the mass fraction of P is the same for both mixtures. For the

P-containing problem two Klug's equations can be written for the intensities of selected non-overlapping peaks of Y and P, respectively:

$$I_{\mathrm{Y}} = I_{\mathrm{Y}}^{\mathrm{o}} \frac{f_{\mathrm{Y}}}{1+ f_{\mathrm{Y}}(1-b_{\mathrm{Y}})} \qquad (6)$$

$$I_{\mathrm{P}} = I_{\mathrm{P}}^{\mathrm{o}} \frac{f_{\mathrm{P}}}{1+ f_{\mathrm{P}}(1-b_{\mathrm{P}})} \qquad (7)$$

where $I_{\mathrm{P}}^{\mathrm{o}}$ denotes the intensity of the selected peak of P in the diffractogram of the pure standard under the conditions of operation and b_{Y}, b_{P} the parameters expressing the absorption effects. The ratio between the above intensities is:

$$\frac{I_{\mathrm{Y}}}{I_{\mathrm{P}}} = \left(\frac{I_{\mathrm{Y}}^{\mathrm{o}}}{I_{\mathrm{P}}^{\mathrm{o}}}\right)\left(\frac{f_{\mathrm{Y}}}{f_{\mathrm{P}}}\right)\left[\frac{1+ f_{\mathrm{P}}(1-b_{\mathrm{P}})}{1+ f_{\mathrm{Y}}(1-b_{\mathrm{Y}})}\right] \qquad (8)$$

In a standard additions experiment, a series of specimens containing a constant mass fraction of P and the sample enriched with known amounts of Y are used. Then, the corresponding series of diffractograms will contain the P- and Y-characteristic peaks. The intensities of these peaks will verify:

$$\frac{I_{\mathrm{Y}}^{*}}{I_{\mathrm{P}}^{*}} = \left(\frac{I_{\mathrm{Y}}^{\mathrm{o}}}{I_{\mathrm{P}}^{\mathrm{o}}}\right)\left(\frac{f_{\mathrm{Y}} + f_{\mathrm{Y}}^{*}}{f_{\mathrm{P}}}\right)\left[\frac{1+ f_{\mathrm{P}}(1-b_{\mathrm{P}}^{*})}{1+(f_{\mathrm{Y}} + f_{\mathrm{Y}}^{*})(1-b_{\mathrm{Y}}^{*})}\right] \qquad (9)$$

Assuming that the mass absorption coefficients b^{*} depends on all the components of the sample but does not vary significantly with their abundances (i.e.: $b_{\mathrm{Y}} = b_{\mathrm{Y}}^{*}; b_{\mathrm{P}} = b_{\mathrm{P}}^{*}$), combining Eqs. (8) and (9) yields:

$$\frac{I_{\mathrm{Y}}^{*}}{I_{\mathrm{P}}^{*}} = \frac{I_{\mathrm{Y}}}{I_{\mathrm{P}}} + \left(\frac{I_{\mathrm{Y}}^{\mathrm{o}}}{I_{\mathrm{P}}^{\mathrm{o}}}\right)\left(\frac{f_{\mathrm{Y}}^{*}}{f_{\mathrm{P}}}\right)\left[\frac{1+ f_{\mathrm{P}}(1-b_{\mathrm{P}}^{*})}{1+(f_{\mathrm{Y}} + f_{\mathrm{Y}}^{*})(1-b_{\mathrm{Y}}^{*})}\right] \qquad (10)$$

This equation corresponds to a polynomial function of the $I_{\mathrm{Y}}^{*} / I_{\mathrm{P}}^{*}$ ratio on the $f_{\mathrm{Y}}^{*} / f_{\mathrm{P}}$ ratio that, when f_{Y}^{*} tends to zero, approaches a straight line given by:

$$\frac{I_Y^*}{I_P^*} \approx \frac{I_Y}{I_P} + \left(\frac{I_Y^o}{I_P^o}\right)\left(\frac{f_Y^*}{f_P}\right)\left[\frac{1+f_P(1-b_P^*)}{1+f_Y(1-b_Y^*)}\right] = \frac{I_Y}{I_P} + \frac{I_Y}{I_P}\left(\frac{f_P}{f_Y}\right)\left(\frac{f_Y^*}{f_P}\right) \qquad (11)$$

This equation predicts that the plots of I_Y^*/I_P^* vs. f_Y^*/f_P tend asymptotically to a straight line of ordinate at the origin I_Y/I_P, and slope $(I_Y/I_P)(f_P/f_Y)$ when f_Y^* tends to zero.

There are other possible particular cases of Eq. (10) of interest. For instance, when $b_Y^* \approx 1; b_P^* \approx 1$, it reduces to:

$$\frac{I_Y^*}{I_P^*} = \frac{I_Y}{I_P} + \left(\frac{I_Y^o}{I_P^o}\right)\left(\frac{f_Y^*}{f_P}\right) \qquad (12)$$

On the contrary, when $b_Y^* >> 1; b_P^* >> 1$, Eq. (10) becomes:

$$\frac{I_Y^*}{I_P^*} = \frac{I_Y}{I_P} + \left(\frac{I_Y^o}{I_P^o}\right)\left(\frac{b_P^*}{b_Y^*}\right)\left(\frac{f_Y^*}{f_Y + f_Y^*}\right) \qquad (13)$$

When $b_Y^* << 1; b_P^* >> 1$, then:

$$\frac{I_Y^*}{I_P^*} = \frac{I_Y}{I_P} + \left(\frac{I_Y^o}{I_P^o}\right)\left(\frac{f_Y^*}{f_P}\right)\left[\frac{-b_P^* f_P}{1+(f_Y + f_Y^*)}\right] \qquad (14)$$

This case corresponds, when $f_Y^* \to 0$, to a straight line of negative slope in the representation of I_Y^*/I_P^* vs. f_Y^*/f_P. Theoretical representations for different values of b_Y^* and b_P^*, according to Eq. (10) are presented as a Supplementary information, Figure S.1.

3.2. ATR-ACR method

Let us consider again the case of the quantification of a solid analyte Y of known spectrum which is present in a solid sample accompanied by interferents X of unknown spectra which present absorption bands overlapped with those of the analyte and an IR-transparent matrix. For quantification purposes, we prepare a sample enriched with a weighted amount of a standard whose spectrum does not overlap with those of the sample and the interferent. Assuming that the matrix does not distort seriously the spectral features of X, Y, and P, the absorbance at a given wavenumber υ will be:

$$A(\upsilon) = \varepsilon_Y(\upsilon) g(\upsilon) c_Y + \varepsilon_X(\upsilon) g(\upsilon) c_X \qquad (15)$$

where ε_J (J = Y, X) denote the specific absorptivity (by mass unit or mol unit) of the different components at the wavenumber υ, c_J their respective concentrations and $g(\upsilon)$ the optical path. In turn, the absorbance of the standard band at a wavenumber υ_P will be:

$$A_P(\upsilon_P) = \varepsilon_P(\upsilon_P) g(\upsilon_P) c_P \qquad (16)$$

$g(\upsilon_P)$ being the optical path at the wavenumber υ_P that in general will differ from $g(\upsilon)$ in the same spectrum. Then, we can obtain the absorbance ratio:

$$\frac{A(\upsilon)}{A_P(\upsilon_P)} = \frac{\varepsilon_Y(\upsilon) g(\upsilon) c_Y + \varepsilon_X(\upsilon) g(\upsilon) c_X}{\varepsilon_P(\upsilon_P) g(\upsilon_P) c_P} \qquad (17)$$

Introducing the mass (or mole) fraction of the analyte in the original sample, f_Y (= $c_Y/(c_X + c_Y)$), Eq. (17) becomes:

$$\frac{A(\upsilon)}{A_P(\upsilon_P)} = \frac{1}{F}\left[\frac{\varepsilon_Y(\upsilon) g(\upsilon)}{\varepsilon_P(\upsilon_P) g(\upsilon_P)} f_Y + \frac{\varepsilon_X(\upsilon) g(\upsilon)}{\varepsilon_P(\upsilon_P) g(\upsilon_P)}(1 - f_Y)\right] \qquad (18)$$

where $F = (c_X + c_Y)/c_P$. This coefficient can be fixed by weighting the amount of original sample ($c_X + c_Y$) and the amount of added internal standard P.

Now, we prepare a series of Y-enriched samples containing a fixed proportion of P to develop a standard additions experiment. Then, Eq. (18) can be rewritten as:

$$\frac{A^*(\upsilon)}{A_P^*(\upsilon_P)} = \frac{1}{F}\left[\frac{\varepsilon_Y(\upsilon) g^*(\upsilon)}{\varepsilon_P(\upsilon_P) g^*(\upsilon_P)}(f_Y + f_Y^*) + \frac{\varepsilon_X(\upsilon) g^*(\upsilon)}{\varepsilon_P(\upsilon_P) g^*(\upsilon_P)}(1 - f_Y - f_Y^*)\right] \qquad (19)$$

c_Y^* being the added concentration of Y and $f_Y^* = c_Y^*/(c_X + c_Y)$.

In general, the optical paths (g-terms) will vary with the entire composition of the

system. Assuming that these terms do not vary significantly in standard additions experiments, we can approximate $g^*(\upsilon)/g^*(\upsilon_P) = k$ (constant). Then, eliminating $\varepsilon_X(\upsilon)g(\upsilon)/\varepsilon_P(\upsilon_P)g^*(\upsilon_P)$ between Eqs. (18) and (19) yields:

$$F\frac{A^*(\upsilon)}{A_P^*(\upsilon_P)} - F\frac{A(\upsilon)}{A_P(\upsilon_P)} = \left(\frac{k\dfrac{\varepsilon_Y(\upsilon)}{\varepsilon_P(\upsilon_P)} - F\dfrac{A(\upsilon)}{A_P(\upsilon_P)}}{1-f_Y}\right) f_Y^* \qquad (20)$$

This equation predicts a linear relationship between F ($A^*(\upsilon)/A_P^*(\upsilon_P)$) and f_Y^*. Since the $\varepsilon_Y(\upsilon)g(\upsilon)/\varepsilon_P(\upsilon_P)g(\upsilon_P)$ ratio can easily be determined from mixtures of weighted amounts of Y- and P-standards, and assuming that the $g(\upsilon)/g(\upsilon_P)$ ratio approximates the same k the value (i.e. $\varepsilon_Y(\upsilon)g(\upsilon)/\varepsilon_P(\upsilon_P)g(\upsilon_P) = k\varepsilon_Y(\upsilon)/\varepsilon_P(\upsilon_P)$), the value of f_Y can be calculated from the slope of the F ($A^*(\upsilon)/A_P^*(\upsilon_P)$) vs. f_Y^* plot as:

$$f_Y = 1 - \left(\frac{k\dfrac{\varepsilon_Y(\upsilon)}{\varepsilon_P(\upsilon_P)} - F\dfrac{A(\upsilon)}{A_P(\upsilon_P)}}{\dfrac{\Delta\left(F\dfrac{A^*(\upsilon)}{A_P^*(\upsilon_P)} - F\dfrac{A(\upsilon)}{A_P(\upsilon_P)}\right)}{\Delta(f_Y^*)}}\right) \qquad (21)$$

Under real conditions, the optical paths will distort the spectral response. Since this distortion (represented by the $g^*(\upsilon)$ variable term) will increase with Y-standard concentration, Eq. (20) will apply for low added concentrations; i.e., the experimental $F(A^*(\upsilon)/A_P^*(\upsilon_P))$ vs. f_Y^* curve will tend asymptotically to a straight line represented by Eq. (20).

4. Results and discussion

4.1. Preliminary XRD test

First we studied the diffractometry of mixtures of NiO and Cr_2O_3 using TiO_2 as the internal standard. Figure 1 compares the X-ray diffractograms of the separate

components and a mixture containing mass fractions of 0.200±0.002 TiO_2, 0.400±0.002 NiO and 0.400±0.002 Cr_2O_3. Figure 2 shows the standard additions graphs obtained by selecting the peaks at 2Θ = 25.3, 33.6, and 43.4 degrees for TiO_2, Cr_2O_3, and NiO, respectively. Taking as a problem sample a mixture containing a mass fraction of NiO of 0.200±0.002, a mass fraction of Cr_2O_3 of 0.600±0.002, and a mass fraction of TiO_2 internal standard of 0.200±0.002, and preparing samples containing the same mass fraction of TiO_2 but with increasing mass fractions of NiO, the resulting representation of I^*_{NiO}/I^*_{TiO2} vs. f^*_{NiO}/f_{TiO2} yields a clearly curved path. The first experimental points can be satisfactorily fitted to a straight line, thus defining an asymptotic linear region (ALR) marked in Fig. 2a. Application of Eq. (11) to these points yields: I^*_{NiO}/I^*_{TiO2} = (0.186±0.002)(f^*_{NiO}/f_{TiO2}) + 0.1956±0.0014 (N = 3, r = 0.99990) which provide for the problem sample f_{NiO} = 0.210±0.003, again in agreement with the nominal value.

The same procedure was used now taking as a problem sample one containing a mass fraction of NiO of 0.600±0.002, a mass fraction of Cr_2O_3 of 0.200±0.002, and a mass fraction of TiO_2 internal standard of 0.200±0.002, now performing standard additions of Cr_2O_3. The corresponding representation of I^*_{Cr2O3}/I^*_{TiO2} vs. f^*_{Cr2O3}/f_{TiO2} is also shown in Figure 2a, yielding almost linear representation using peak heights. Fitting the entire set of experimental values to a straight line, one obtains a slope of 0.40±0.02 and an ordinate at the origin of 0.398±0.022 (N = 5, r = 0.997) resulting in a value of f_{Cr2O3} = 0.20±0.02, in agreement with the expected value.

In order to refine the calculations, Eq. (11) can be rewritten as:

$$G = \frac{\frac{I^*_Y}{I^*_P} - \frac{I_Y}{I_P}}{\frac{f^*_Y}{f_P}} = \left(\frac{I_Y}{I_P}\right)\left(\frac{f_P}{f_Y}\right) \qquad (22)$$

Taking into account that Eq. (11) reflects the limiting tendency of Eq. (10) when f^*_Y/f_P tends to zero, Eq. (21) predicts that plots of G vs. f^*_Y/f_P should provide a curve tending a horizontal line at $G = (I_Y/I_P)(f_P/f_Y)$. Figure 2b shows the representation of

G vs. f^*_{NiO} / f_{TiO2} for the precedent experiment of standard additions of NiO. In agreement with the expectances, the curved path tends to a horizontal line at G = 0.190±0.002 when $f^*_{NiO} / f_{TiO2} \to 0$. Using the I_{NiO}/I_{TiO2} value determined for the sample (0.196±0.002), one can re-calculate the value of f_{TiO2}/f_{NiO} (0.969±0.003), the f_{NiO} value is of 0.206±0.006, improving the value previously calculated.

Interestingly, experimental data can in principle be fitted to empirical relationships of the type:

$$\frac{I^*_Y}{I^*_P} = m + n\left(\frac{f^*_Y}{f_P}\right) + q\left(\frac{f^*_Y}{f_P}\right)^2 \qquad (23)$$

where m, n, and q are adjustable parameters which can be calculated from the polynomial fit of data equivalent to the I_Y/I_P and $(I_Y/I_P)(f_P/f_Y)$ terms in Eq. (11). The obtained data agree satisfactorily with those previously indicated. A comparison of the statistical parameters determined for the NiO sample using the polynomial fitting and the linear fit of the asymptotic line is summarized in Table 1. A second preliminary test, carried out using mixtures of MgO and SiO_2 again taking TiO_2 as an internal standard is presented in Supplementary information, Figures S.2 and S.3.

The analysis of errors is presented as an Appendix. Under ordinary conditions, and assuming $\Delta I/I_o$ values below 2%, one can estimate detection limits corresponding to mass fractions of the analyte around 2%, which can be considered as a satisfactory value for XRD measurements.

4.2. XRD quantification of sodium and potassium feldspars

A more complex example of application used mixtures of sodium and potassium feldspars (NaFeld and Kfeld in the following), plagioclase minerals whose extreme members are albite, $NaAlSi_3O_8$ and orthoclase, $KAlSi_3O_8$. This is a case of practical interest in ceramic science that is made difficult by the fact that there is no disposal of pure chemicals, so that the composition of the available mineral standards does not fit to

the theoretical chemical composition of the respective compound. This can be seen in Table 2, where the certified composition of the NaFeld and KFeld mineral standards is given. Based on these data, one can estimate that the NaFeld standard contains 72.24 %wt of albite and 8.7 %wt of orthoclase and that the KFeld standard contains 33.56 %wt of albite and 56.85 %wt of orthoclase.

Figure 3 depicts the X-ray diffractograms of a) NaFeld, b) KFeld, c) a 10.0±0.1 %wt TiO_2 plus 20.0±0.1 %wt NaFeld plus 70.0±0.1 %wt KFeld mixture. This last was taken as a problem sample. To apply the ACR method to determine the concentration of NaFeld, the peak at 2Θ = 27.5 deg. for NaFeld and the peak at 2Θ = 25.3 deg. for TiO_2 were used. As can be seen in Figure 4a, the resulting $I^*_{\mathrm{NaFeld}} / I^*_{\mathrm{TiO2}}$ vs. $f^*_{\mathrm{NaFeld}} / f_{\mathrm{TiO2}}$ plot describes a curved path for which the tangent at $f^*_{\mathrm{NaFeld}} / f_{\mathrm{TiO2}} \rightarrow 0$ can be fitted to a straight line of equation $I^*_{\mathrm{NaFeld}} / I^*_{\mathrm{TiO2}}$ = (0.2032±0.0009)($f^*_{\mathrm{NaFeld}} / f_{\mathrm{TiO2}}$) + 0.4006±0.0012 ($N$ = 3; r = 99998), yielding a value of f_{NaFeld} in the problem sample of 0.197±0.004, in close agreement with the expected result. This corresponds to a 'true' albite fraction of 0.142±0.004. Applying the polynomial fit to the curve in Figure 4a one obtains $I^*_{\mathrm{NaFeld}} / I^*_{\mathrm{TiO2}} = 0.386 + 0.193\, f^*_{\mathrm{NaFeld}} / f_{\mathrm{TiO2}} + 0.0082 \left(f^*_{\mathrm{NaFeld}} / f_{\mathrm{TiO2}}\right)^2$ (r = 0.9999), finally resulting in an albite fraction of 0.145±0.006.

In the case of KFeld, the problem mixture was composed by 10.0±0.1 %wt TiO_2 plus 70.0±0.1 %wt NaFeld plus 20.0±0.1 %wt KFeld. In this case, the better results were obtained using peak intensity measurements at 2Θ = 45.2 deg for KFeld. The corresponding representation is depicted in Figure 4b. Now, the equation of the tangent at $f^*_{KFeld} / f_{TiO2} \rightarrow 0$ can be fitted to a straight line of equation $I^*_{\mathrm{KFeld}} / I^*_{\mathrm{TiO2}}$ = (0.0230±0.0009)($f^*_{\mathrm{KFeld}} / f_{\mathrm{TiO2}}$) + 0.0473±0.0016 ($N$ = 3; r = 9990). This equation leads to a value of f_{KFeld} in the problem sample of 0.206±0.004, again in agreement with the nominal result corresponding, after correction of the standard composition, to 0.116±0.004. Applying the polynomial fit to the curve in Figure 4b one obtains $I^*_{\mathrm{KFeld}} / I^*_{\mathrm{TiO2}} = 0.0456 + 0.0221\, f^*_{\mathrm{KFeld}} / f_{\mathrm{TiO2}} + 0.0021 \left(f^*_{\mathrm{KFeld}} / f_{\mathrm{TiO2}}\right)^2$ (r = 0.997), finally resulting in an orthoclase fraction of 0.116±0.006. Table 3 summarizes the results for the quantification of feldspars using the XRD-ACR method.

The above results suggest that the XRD-ACR method can be used to quantify individual components in a variety of mixtures of crystalline components providing that the individual diffraction patterns provide non-overlapping signals. The method may be distorted, however, by non-crystallinity and intense absorption effects whose influence should be matter of future research.

4.3. ATR-FTIR quantification of sodium and potassium feldspars

Figure 5 shows the ATR-FTIR transmittance spectra of a) $KHCO_3$, b) KFeld, c) NaFeld, and d) a mixture of KFeld plus NaFeld spiked with $KHCO_3$ resulting in mass percentages of 43.5, 34.8, and 21.7 %wt, respectively. This last is an illustrative example of a mixture containing similar percentages of NaFeld and KFeld, the most favorable case for quantification. Apart from characteristic OH bands around 2500 cm^{-1}, the spectrum of $KHCO_3$ display carbonate bands at 661, 700, 827, 971, 1387/1400 and 1620 cm^{-1}. In turn, both KFeld and NaFeld yield overlapping bands between 800 and 1200 cm^{-1} dominated by the asymmetric stretching vibration of the SiO units with a maximum of absorption at 1080 cm^{-1}, accompanied by less intense bands assigned to the symmetric SiO stretch at 800 and 780 cm^{-1}, and the symmetric and asymmetric SiO bending modes at 695, 520, and 450 cm^{-1}. For quantification purposes, we selected the SiO band at 1150 cm^{-1} and the carbonate band at 1400 cm^{-1} where only one of the components ($KHCO_3$ or feldspars) absorb.

We prepared as a sample a mixture of KFeld and NaFeld containing 22.2 %wt of KFeld and prepared a modified sample and a series of standards all containing a 21.7 %wt of $KHCO_3$. Figure 6 compares the spectra of the $KHCO_3$-enriched sample and the $KHCO_3$-enriched specimen after the addition of a standard of KFeld. The base line was defined as that joining the two minima at about 1250 and about 850 cm^{-1}. This line and criteria for absorbance measurements are depicted in Fig. 6. Figure 7a depicts the representation of $F(A^*_{\mathrm{KFeld}}/A^*_{\mathrm{KHCO3}}) - F(A_{\mathrm{KFeld}}/A_{\mathrm{KHCO3}})$ vs. f^*_{KFeld} obtained from absorbance measurements at 1150 cm^{-1} (A^*_{KFeld}) and 1400 cm^{-1} (A^*_{KHCO3}) corresponding to weighted mixtures with F = 0.277±0.001. In agreement with theoretical expectances, the representation defines a curved path tending asymptotically to a straight line at low

f^*_{KFeld} values intersecting the *y*-axis at the absorbance ratio of the $KHCO_3$-enriched sample. In turn, experiments at KFeld plus $KHCO_3$ mixtures of known composition permitted to determine $\varepsilon_{KFeld}/\varepsilon_{KHCO3}$= 1.610±0.005. Taking the asymptotic straight line defined by the first four experimental data point (asymptotic linear region marked as ALR in Fig. 7a), of equation $F(A^*_{KFeld}/A^*_{KHCO3}) - F(A_{KFeld}/A_{KHCO3})$ = (1.12±0.02) f^*_{KFeld} + 0.003±0.04 (r = 0.9995), one obtains f_{KFeld} = 0.220±0.006, in close agreement with the nominal value (0.222±0.002).

Similar results were obtained for a sample consisting of a mixture of KFeld and NaFeld containing 22.2 %wt of NaFeld which was now taken as the analyte. The sample and the sample plus NaFeld standards were prepared containing a 21.7 %wt of $KHCO_3$, thus resulting in F = 0.277±0.001. Figure 7b shows the corresponding representation of $F(A^*_{NaFeld}/A^*_{KHCO3}) - F(A_{NaFeld}/A_{KHCO3})$ vs. f^*_{NaFeld}. Here, a curved path tending to a straight line at low f^*_{NaFeld} values was obtained. The equation of the asymptotic line taken the first experimental data points fits to $F(A^*_{NaFeld}/A^*_{KHCO3}) - F(A_{NaFeld}/A_{KHCO3})$ = (–1.77±0.008) f^*_{NaFeld} + 0.07±0.07 (r = 0.9994). The slope value, combined with the value of the $\varepsilon_{NaFeld}/\varepsilon_{KHCO3}$ratio (0.529) determined from ATR-FTIR spectra recorded in binary NaFeld plus $KHCO_3$ mixtures, yields f_{NaFeld} = 0.221±0.007, in close agreement with the expected value (0.222±0.002).

These results indicate that the ATR-ACR method provides satisfactory results for the quantification of an individual analyte in the presence of unknown matrices. It is pertinent to note that in the case of feldspars, as occurring in XRD, the studied compositions refer to the nominal composition of the standards. The analysis of errors is similar to that for the XRD-ACR method and is presented as an Appendix. Under the experimental conditions described in the next section, the detection limit for the analyte can be evaluated as around 2%, which is a reasonable value for ATR-FTIR analysis.

5. Conclusions

Two methods devoted to quantify individual components in an unknown crystalline solid matrix based on either XRD and ATR-FTIR data are described. Both methods are based on the addition of a known amount of an internal standard of known diffraction pattern or spectrum with no overlapping bands with those of the components of the problem system and the determination of the peak intensity ratios of signals characteristic of the problem components relative to a peak of the standard. Performing standard additions of the component to quantify to mixtures containing a constant proportion of the internal standard, the above peak current ratio tends asymptotically to a linear variation with the ratio between the added amount of problem standard and the amount of internal standard allowing for the calculation of the concentration of the problem component with no need of independent knowledge of the absorption parameters of the matrix.

In the case of XRD analysis, the application of the Klug's equation permits to compensate the effect of the absorption of the unknown matrix, the resulting XRD-ACR method being satisfactorily applied to binary mixtures of Cr_2O_3 plus NiO, and sodium and potassium feldspars, respectively, using TiO_2 (anatase) as the internal standard. In the case of ATR-FTIR, the ATR-ACR method can be applied to the determination of an analyte in the presence of an unknown matrix whose absorption bands overlap with those of the analyte. This method was satisfactorily applied to solve mixtures of sodium and potassium feldspars using $KHCO_3$ as internal standard, thus suggesting the suitability of the method to study a variety of systems.

Acknowledgements: Financial support from the Project CTQ2017-85317-C2-1-P (*Ministerio de Economía, Industria y Competitividad* (MINECO), *Fondo Europeo de Desarrollo Regional* (ERDF) and *Agencia Estatal de Investigación* (AEI)), is gratefully acknowledged.

Appendix. Analysis of errors

The proposed methods have the intrinsic advantage that, apart from those associated to weighting, only errors associated to peak intensity (or peak area) measurements have to be accounted, thus avoiding, in the case of XRD, the account of errors associated to the estimate of absorption coefficients. To estimate errors in the XRD-ACR method based on Eq. (11) an approximate treatment can be taken assuming that the uncertainty (in the following represented by Δ) in the mass fraction of a given analyte relative to the internal standard depends on those of the intensities of the respective diffraction peaks (XRD-ACR) and those of the mass fraction of the standards, both represented in the following as *S*. Then, Eq. (11) can be rewritten as:

$$\frac{f_{\mathrm{Y}}}{f_{\mathrm{P}}}=\frac{\frac{\mathrm{I}_{\mathrm{Y}}^{*}}{\mathrm{I}_{\mathrm{P}}^{*}}-\frac{I_{\mathrm{Y}}}{I_{\mathrm{P}}}}{\left(\frac{I_{\mathrm{Y}}}{I_{\mathrm{P}}}\right)\left(\frac{f_{\mathrm{Y}}^{*}}{f_{\mathrm{P}}}\right)}=\frac{\left(\frac{I_{\mathrm{Y}}^{*}}{I_{\mathrm{P}}^{*}}\right)\left(\frac{I_{\mathrm{P}}}{I_{\mathrm{Y}}}\right)-1}{\frac{f_{\mathrm{Y}}^{*}}{f_{\mathrm{P}}}}=\frac{\frac{S_{\mathrm{Y}}^{*}}{S_{\mathrm{P}}^{*}}}{\frac{f_{\mathrm{Y}}^{*}}{f_{\mathrm{P}}}} \qquad \text{(A.1)}$$

Then, the usual treatment of error's propagation yields:

$$\left(\frac{\Delta(f_{\mathrm{Y}}/f_{\mathrm{P}})}{f_{\mathrm{Y}}/f_{\mathrm{P}}}\right)=\left(\frac{\Delta(f_{\mathrm{Y}}^{*}/f_{\mathrm{P}})}{f_{\mathrm{Y}}^{*}/f_{\mathrm{P}}}\right)+\left(\frac{\Delta(S_{\mathrm{Y}}^{*}/S_{\mathrm{P}}^{*})}{S_{\mathrm{Y}}^{*}/S_{\mathrm{P}}^{*}}\right) \qquad \text{(A.2)}$$

In the case of the ATR-ACR method, Eq. (20) leads to:

$$f_{\mathrm{Y}}=1-\left(\frac{k\frac{\varepsilon_{\mathrm{Y}}(\upsilon)}{\varepsilon_{\mathrm{P}}(\upsilon_{\mathrm{P}})}-F\frac{A(\upsilon)}{A_{\mathrm{P}}(\upsilon_{\mathrm{P}})}}{F\frac{A^{*}(\upsilon)}{A_{\mathrm{P}}^{*}(\upsilon_{\mathrm{P}})}-F\frac{A(\upsilon)}{A_{\mathrm{P}}(\upsilon_{\mathrm{P}})}}\right)f_{\mathrm{Y}}^{*}=1-\frac{Q^{*}(\upsilon)}{Q_{\mathrm{P}}(\upsilon_{\mathrm{P}})}f_{\mathrm{Y}}^{*} \qquad \text{(A.3)}$$

where we introduce a *Q*-function depending on the measured absorbances. Although the *Q*-function in Eq. (A.3) is more complicated than the *S*-function in Eq. (A.2), the theory of error propagation can in principle be reasonably applied using similar approximations.

One of the aspects of relevant interest is to estimate the detection limit attainable with the

method. For this purpose, a first plausible assumption is, for simplicity, that the uncertainty in the individual measurements of the peak intensities, ΔS, is the same in all cases. Then:

$$\left(\frac{\Delta(S_{\mathrm{Y}}^{*}/S_{\mathrm{P}}^{*})}{S_{\mathrm{Y}}^{*}/S_{\mathrm{P}}^{*}}\right)=\Delta S\left(\frac{1}{S_{\mathrm{Y}}^{*}}+\frac{1}{S_{\mathrm{P}}^{*}}\right) \qquad \text{(A.4)}$$

Thinking in the detection of a low proportion of the analyte Y, it is reasonable to assume that the sum of the peak intensities of the problem compound and the standard remain approximately constant and equal to a value S_{o}. Then, the value of the peak intensity ratio, $\xi\,(=S_{\mathrm{Y}}^{*}/S_{\mathrm{P}}^{*})$ can be related with the relative error in that ratio by means of the relationship:

$$\left(\frac{\Delta(S_{\mathrm{Y}}^{*}/S_{\mathrm{P}}^{*})}{S_{\mathrm{Y}}^{*}/S_{\mathrm{P}}^{*}}\right)=\frac{\Delta S}{S_{\mathrm{o}}}\frac{(1+\xi)^{2}}{\xi} \qquad \text{(A.5)}$$

Here, the ratio $\Delta S/S_{\mathrm{o}}$ represents an averaged value of the relative uncertainty in peak intensity measurements. If this ratio is constant, the uncertainty in the peak intensity ratio tends to a minimum value for $\xi = 1$; i.e., when the height of the analyte and the standard peaks is the same. This treatment can be extended to the analyte to standard mass ratio so that, introducing and averaged value of the uncertainties in these measurements, $\Delta f/f_{\mathrm{o}}$, and the mass fraction ratio $\zeta\,(=f_{\mathrm{Y}}^{*}/f_{\mathrm{P}}^{*})$, one obtains:

$$\left(\frac{\Delta(f_{\mathrm{Y}}^{*}/f_{\mathrm{P}})}{f_{\mathrm{Y}}^{*}/f_{\mathrm{P}}}\right)=\frac{\Delta f}{f_{\mathrm{o}}}\frac{(1+\zeta)^{2}}{\zeta} \qquad \text{(A.6)}$$

This relationship leads again to predict a minimum uncertainty for a mass fraction ratio equal to one that, obviously, is not a situation of practical interest. Combining the equations (A.5) and (A.6) yields:

$$\left(\frac{\Delta(f_{\mathrm{Y}}/f_{\mathrm{P}})}{f_{\mathrm{Y}}/f_{\mathrm{P}}}\right)=\frac{\Delta I}{I_{\mathrm{o}}}\frac{(1+\xi)^{2}}{\xi}+\frac{\Delta f}{f_{\mathrm{o}}}\frac{(1+\zeta)^{2}}{\zeta} \qquad \text{(A.7)}$$

Figure S.4 depicts the variation of the relative uncertainty in the mass fraction ratio, $\Delta(f_Y/f_P)/(f_Y/f_P)$, on ζ for ξ = 1.0 assuming $\Delta f/f_o$ = 1% , a reasonable value taking into account the accuracy in weighting, and taking different values of the $\Delta S/S_o$ ratio.

References

[1] L.-M. Shillito, M.J. Almond, J. Nicholson, M. Pantos, W. Matthews, Rapid characterisation of archaeological midden components using FT-IR spectroscopy, SEM–EDX and micro-XRD. Spectrochim. Acta A 73 (2009) 133-139.

[2] L. Zhirong, Md. Azhar Udin, S. Zhanxue, FT-IR and XRD analysis of natural Na-bentonite and Cu(II)-loaded Na-bentonite. Spectrochim. Acta A 79 (2011) 1013-1016.

[3] G. Nirmala, G. Viruthagiri, FT-IR characterization of articulated ceramic bricks with wastes from ceramic industries. Spectrochim. Acta A 126 (2014) 129-134.

[4] E. Anderson, M.J. Almond, W. Matthews, Analysis of wall plasters and natural sediments from the Neolithic town of Çatalhöyük (Turkey) by a range of analytical techniques. Spectrochim. Acta A 136 (2014) 326-334.

[5] A. Rahfeld, R. Kleeberg, R. Möckel, J. Gutzmer, Quantitative mineralogical analysis of European Kupferschiefer ore. Miner. Eng. 115 (2018) 21-32.

[6] S. Lafon, J.-L. Rajot, S.C. Alfaro, A. Gaudichet, Quantification of iron oxides in desert aerosol, Atmosph. Environ. 38 (2004) 1211–1218.

[7] J.L. Díaz-Hernández, J.D. Martín-Ramos, A. López-Galindo, Quantitative analysis of mineral phases in atmospheric dust deposited in the south-eastern Iberian Peninsula. Atmos. Envir. 45 (2011) 3015–3024.

[8] M. Dumon, A. Regassa Tolossa, B. Capon, C. Detavernier, E. Van Ranst, Quantitative clay mineralogy of a Vertic Planosol in southwestern Ethiopia: Impact on soil formation hypotheses, Geoderma, 214-215 (2014) 184–196.

[9] S. Casetou-Gustafson, S. Hillier, C. Akselsson, M. Simonsson, J. Stendahl, B.A. Olsson, Comparison of measured (XRPD) and modeled (A2M) soil mineralogies: A study of some Swedish forest soils in the context of weathering rate predictions. Geoderma 310 (2018) 77-88.

[10] B.M. Butler, S.M. O'Rourke, S. Hillier, Using rule-based regression models to predict and interpret soil properties from X-ray powder diffraction data, Geoderma 329 (2018) 43–53.

[11] J. Dietel, K. Ufer, S. Kaufhold, R. Dorhmann, Crystal structure model development for soil clay minerals – II. Quantification and characterization of hydroxy-interlayered smectite (HIS) using the Rietveld refinement technique, Geoderma 347 (2019) 1–12.

[12] B.M. Butler, A.M. Sila, K.D. Shepherd, M. Nyambura, C.J. Gilmore, N. Kourkoumelis, S. Hillier, Pre-treatment of soil X-ray powder diffraction data for cluster analysis, Geoderma 337 (2019) 413–424.

[13] M. Ostrooumov, M.S. Hernández-Beranl, Mineralogical composition of the meteorite El Pozo (Mexico): A Raman, infrared and XRD study. Spectrochim. Acta A 83 (2011) 437–443.

[14] M. Ostroounov, A Raman, IR and XRD analysis of the deterioration on historical monuments: Case study from Mexico, Spectrochim. Acta A 73 (2009) 498–504.

[15] G.W. Brindley, Quantitative X-Ray mineral analysis of clays. In G.W. Brindley and G. Broen, eds. Crystal Structures of Clay Minerals and their X-Ray identification. Mineralogical Society, London, 1980, pp. 411–438.

[16] D.L. Bish, S.A. Howard, Quantitative phase analysis using the Rietveld method. J. Appl. Cryst. 21 (1988) 86–91.

[17] M. Kahle, M. Kleber, R. Jahn, Review of XRD-based quantitative analyses of clay minerals in soils: the suitability of mineral intensity factors, Geoderma 109 (2002) 191–205.

[18] X. Zhou, D. Liu, H. Bu, L. Deng, H. Liu, P. Yuan, P. Du, H. Song, XRD-based quantitative analysis of clay minerals using reference intensity ratios, mineral intensity factors, Rietveld, and full pattern summation methods: A critical review, Solid Herat Sci. 3 (2018) 16–29.

[19] F.H. Chung, Quantitative Interpretation of X-Ray Diffraction Patterns of Mixtures. I. Matrix-Flushing Method for Quantitative Multicomponent Analysis, J. Appl. Cryst. 7 (1974) 519–525.

[20] F.H. Chung, Quantitative Interpretation of X-Ray Dif-fraction Patterns of Mixtures. II. Adiabatic Principle of X- Ray Diffraction Analysis of Mixtures, J. Appl. Cryst. 7 (1974) 526–531.

[21] C.R. Hubbard, E.H. Evans, D.K. Smith, The Reference Intensity Ratio, I/Ic, for Computer Simulated Powder Patterns, J. Appl. Cryst. 9 (1976) 169–174.

[22] D.L. Bish, S.J. Chipera, Problems and Solutions in Quantitative Analysis of Complex Mixtures by X-Ray Powder Diffraction, Adv. X-Ray Anal. 31 (1988) 295–308.

[23] S.J. Chipera, D.L. Bish, FULLPAT: A Full-Pattern Quantitative Analysis Program for X-Ray Powder Dif- fraction Using Measured and Calculated Patterns, J. Appl. Cryst. 35 (2002) 744–749.

[24] H.P. Klug, L.E. Alexander, X-Ray Diffraction Procedures for Polycrystalline and Amorphous Materials, John Wiley & Sons, New York, 1974.

[25] S. Kaufhold, M. Hein, R. Dohrmann, K. Ufer, Quantification of the mineralogical composition of clays using FTIR spectroscopy. Vib. Spectrosc. 59 (2012) 29–39.

[26] D.W. Vidrine, Mid-infrared Spectroscopy in Chemical Process Analysis, in Spectroscopy in Process Analysis, J.M. Chalmers, Ed. Sheffield Academic Press, Sheffield (2000) pp. 96–138.

[27] J.M. Chalmers, Mid-infrared Spectroscopy: Anomalies, Artifacts and Common Errors, in Anomalies, Artifacts and Common Errors in Using Vibrational Spectroscopy Techniques, J.M. Chalmers Edit. John Wiley & Sons, New York, 2002, pp. 2327–2347.

[28] F. Bosch-Reig, J.V. Gimeno-Adelantado, M.C.M. Moya-Moreno, FTIR quantitative analysis of calcium carbonate (calcite) and silica (quartz) mixtures using the constant ratio method. Application to geological samples. Talanta 58 (2002) 811–821.

[29] F. Bosch-Reig, J.V. Gimeno-Adelantado, F. Bosch-Mossi, A. Doménech-Carbó, Quantification of minerals from ATR-FTIR spectra with spectral interferences using the MRC method. Spectrochim. Acta A 181 (2017) 7–12.

[30] S.Kr. Das, K. Dana, Differences in densification behaviour of K- and Na-feldspar-containing porcelain bodies. Thermochim. Acta 406 (2003) 199–206.

[31] A. Pietrodangelo, R. Salzano, E. Rantica, C. Perrino, Characterisation of the local topsoil contribution to airborne particulate matter in the area of Rome (Italy). Source profiles. Atm. Envir. 69 (2013) 1–14.

[32] V. Ramasamy, K. Paramasivam, G. Suresh, M.T. Jose, Function of minerals in the natural radioactivity level of Vaigai River sediments, Tamilnadu, India – Spectroscopical approach. Spectrochim. Acta A 117 (2014) 340–350.

[33] M. Dumariska-Slowik, A. Pieczka, W. Heflik, M. Sikorska, Cancrinite from nepheline syenite (mariupolite) of the Oktiabrski massif, SE Ukraine, and its growth history. Spectrochim. Acta A 157 (2016) 211–219.

[34] R. Ravisankar, G. Raja Annamalai, A. Naseerutheen, A Chandrasekaran, M.V.R. Prasad, K.K. Satpathy, C. Maheswaran, Analytical characterization of recently excavated megalithic sarcophagi potsherds in Veeranam village, Tiruvannamalai dist., Tamilnadu, India. Spectrochim. Acta A 115 (2013) 845–853.

[35] G. Raja Annamalai, R. Ravisankar, A. Rrajalakshmi, A Chandrasekaran, K. Rajan, Spectroscopic characterization of recently excavated archaeological potsherds from Tamilnadu, India with multi-analytical approach. Spectrochim. Acta A 123 (2014) 112–118.

[36] R. Ravisankar, A. Naseerutheen, G. Raja Annamalai, A Chandrasekaran, A. Rrajalakshmi, K.V. Kanagasapathy, M.V.R. Prasad, K.K. Satpathy, The analytical investigations of ancient pottery from Kaveripakkam, Vellore dist, Tamilnadu by spectroscopic techniques. Spectrochim. Acta A 121 (2014) 457–463.

[37] P. Ballirano, C. De Vito, L. Medeghini, S. Mignardi, V. Ferrini, P. Matthiae, D. Bersani, P.P. Lottici. A combined use of optical microscopy, X-ray powder diffraction

and micro-Raman spectroscopy for the characterization of ancient ceramic from Ebla (Syria), Ceram. Int. 40 (2014) 16409–16419.

[38] C. De Vito, L. Medeghini, S. Mignardi, D. Orlandi, L. Nigro, F. Spagnoli, P.P. Lottici, D. Bersani, Technological fingerprints of Black-Gloss Ware from Motya (Western Sicily, Italy), Appl. Clay Sci. 88–89 (2014) 202–213.

Table 1. Composition determined for the problem samples described in the text for NiO plus Cr_2O_3 mixtures using TiO_2 as the internal standard. a) fitting the first experimental points to a straight line as represented in Figure 3; b) using the representation such as in Figure 4; c) using the polynomial fit of the entire set of data.

Analyte	f_P **nominal**	f_P^a	f_P^b	f_P^c
NiO	0.200±0.002	0.210±0.03	0.206±0.006	0.208±0.006
Cr_2O_3	0.200±0.002	0.20±0.02	0.19±0.02	0.20±0.02

Table 2. Certified composition of the NaFeld and KFeld standards used in this study. NaFeld: sodium feldspar (LGC Standards, BCS-CRM Nº 375/1); KFeld: potassium feldspar (NCS DC 61102, China National Analysis Center for Iron and Steel); nd non-detected; ^{teor} theoretical values for albite and orthoclase, respectively; ^{est} composition in albite and orthoclase estimated for the used standards.

%wt	**NaFeld**	**Albite^{teor}**	**KFeld**	**Orthoclase^{teor}**
SiO_2	69.26	68.741	66.26	64.764
TiO_2	0.313		0.048	
Al_2O_3	17.89	19.440	18.63	18.315
Fe_2O_3	0.291		0.19	
Fe_2O_3T	nd		nd	
Na_2O	8.89	11.820	3.69	
K_2O	1.47		9.60	17.047
CaO	0.78		0.76	
MgO	0.180		0.054	
P_2O_5	0.226		nd	
LOI	0.72		0.86	
		Estimation^{est}		**Estimation^{est}**
		Albite		**Orthoclase**
NaFeld		72.24		33.56
KFeld		8.70		56.85

Table 3. Composition determined for the problem samples described in the text using the XRD-ACR[a,b] and the ATR-ACR[c,d] methods for mixtures of NaFeld and KFeld using TiO_2 as the internal standard by means of: [a,c] linear fit of the first data points (Fig. 5a); [b,d] polynomial fit (Fig. 5a).

Analyte	f_P **nominal**	f_P[a]	f_P[b]	f_P **nominal**	f_P[c]	f_P[d]
NaFeld	0.200±0.002	0.197±0.004	0.203±0.006	0.222±0.002	0.220±0.006	0.224±0.008
KFeld	0.200±0.004	0.206±0.006	0.216±0.008	0.222±0.002	0.221±0.007	0.226±0.010
Albite	0.144±0.002	0.142±0.004	0.146±0.006	0.159±0.002	0.158±0.009	0.160±0.008
Orthoclase	0.114±0.004	0.116±0.006	0.123±0.008	0.126±0.004	0.126±0.008	0.128±0.010

Figures

Figure 1. X-ray diffractograms of a) TiO_2, b) NiO, c) Cr_2O_3 and d) a mixture containing mass fractions of 0.200±0.002 TiO_2, 0.400±0.002 NiO and 0.400±0.002 Cr_2O_3. (* TiO_2, $^{\Delta}$ NiO and $^{\square}$ Cr_2O_3)

Figure 2. a) Plots of I^*_{ox} / I^*_{TiO2} vs. f^*_{ox} / f_{TiO2} (ox = Cr_2O_3, NiO) from XRD data in standard additions experiments using TiO_2 as the internal standard. Peak intensity measurements at 2Θ = 25.3, 33.6, and 43.4 degrees for TiO_2, Cr_2O_3, and NiO, respectively. b) Representation of *G* vs. f^*_{NiO} / f_{TiO2} for standard additions of NiO to the TiO_2 plus Cr_2O_3 plus NiO mixture described in the text, corresponding to data in Figure 2. ALR denotes the asymptotic linear region.

Figure 3. X-ray diffractograms of a) NaFeld, b) KFeld, c) a 10.0 %wt TiO_2 plus 70.0%wt NaFeld plus 20.0 %wt KFeld mixture. (* TiO_2, $^{\Delta}$ NaFeld and $^{\square}$ KFeld)

Figure 4. Plots of: a) $I^*_{NaFeld} / I^*_{TiO2}$ vs. f^*_{NaFeld} / f_{TiO2}, and b) I^*_{KFeld} / I^*_{TiO2} vs. f^*_{KFeld} / f_{TiO2}, for standard additions of a) NaFeld, and b) KFeld, to the problem mixtures described in the text. From XRD data in standard additions experiments using TiO_2 as the internal standard using peak intensity measurements at 2Θ = 25.3, 27.5, and 45.2 degrees for TiO_2, NaFeld, and KFeld, respectively. ALR: asymptotic linear region taken for applying Eq. (11).

Figure 5. ATR-FTIR transmittance spectra of a) $KHCO_3$, b) KFeld, c) NaFeld, d) a mixture of KFeld (43.5 %wt), NaFeld (34.8 %wt) plus $KHCO_3$ (21.7 %wt). The continuous (green) arrow marks the carbonate band at 1400 cm^{-1} and the discontinuous (red) arrow the silicate band at 1150 cm^{-1} used for calculations.

Figure 6. ATR-FTIR transmittance spectra of a) $KHCO_3$–enriched sample plus KFeld standard specimen containing 60.9 %wt KFeld, 17.4 %wt NaFeld, and 21.7 %wt $KHCO_3$ and b) $KHCO_3$–enriched sample (resulting composition a mixture of 17.4 %wt KFeld, 60.9 %wt NaFeld, and 21.7 %wt $KHCO_3$). The criteria for defining base lines and absorbance measurements are marked by dotted lines and double arrows,

respectively.

Figure 7. Plots of: a) $F(A^*_{\mathrm{KFeld}}/A^*_{\mathrm{KHCO3}}) - F(A_{\mathrm{KFeld}}/A_{\mathrm{KHCO3}})$ vs. f^*_{KFeld}, and b) $F(A^*_{\mathrm{NaFeld}}/A^*_{\mathrm{KHCO3}}) - F(A_{\mathrm{NaFeld}}/A_{\mathrm{KHCO3}})$ vs. f^*_{NaFeld}, for standard additions of a) KFeld, and b) NaFeld, to the problem samples described in the text. From absorbance measurements at 1150 cm^{-1} (for both KFeld and NaFeld) and 1400 cm^{-1} (for $KHCO_3$) in ATR-FTIR spectra in standard additions experiments using $KHCO_3$ as the internal standard. ALR: asymptotic linear region taken for applying Eq. (20).

Figure 1.

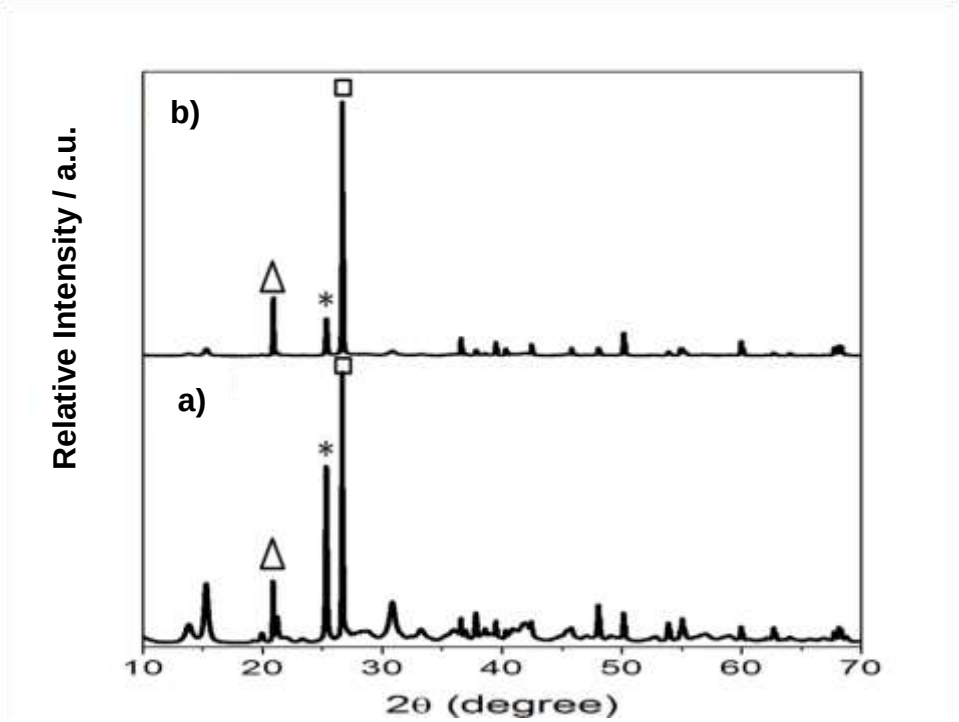

Figure 2.

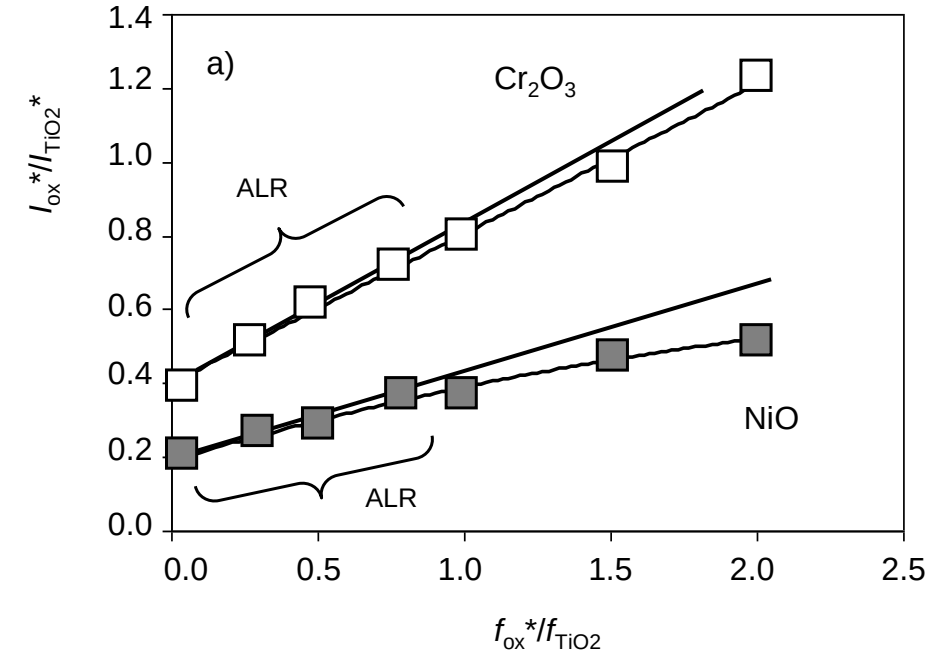
a)
Cr_2O_3
NiO
ALR
ALR
I_{ox}*/I_{TiO2}*
f_{ox}*/f_{TiO2}
1.4
1.2
1.0
0.8
0.6
0.4
0.2
0.0
0.0
0.5
1.0
1.5
2.0
2.5

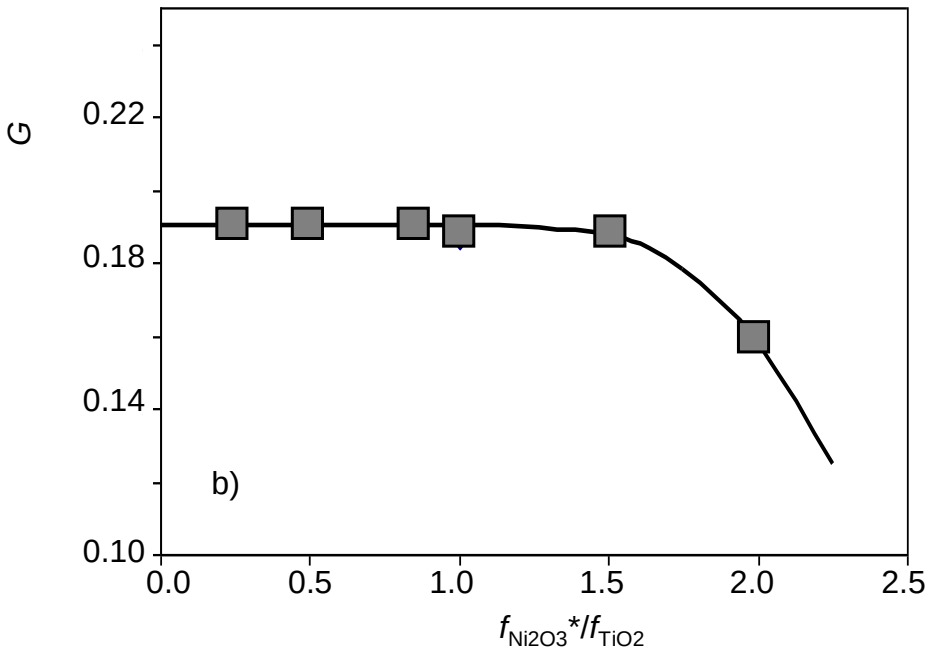
G
b)
f_{Ni2O3}*/f_{TiO2}
0.22
0.18
0.14
0.10
0.0
0.5
1.0
1.5
2.0
2.5

Figure 3.

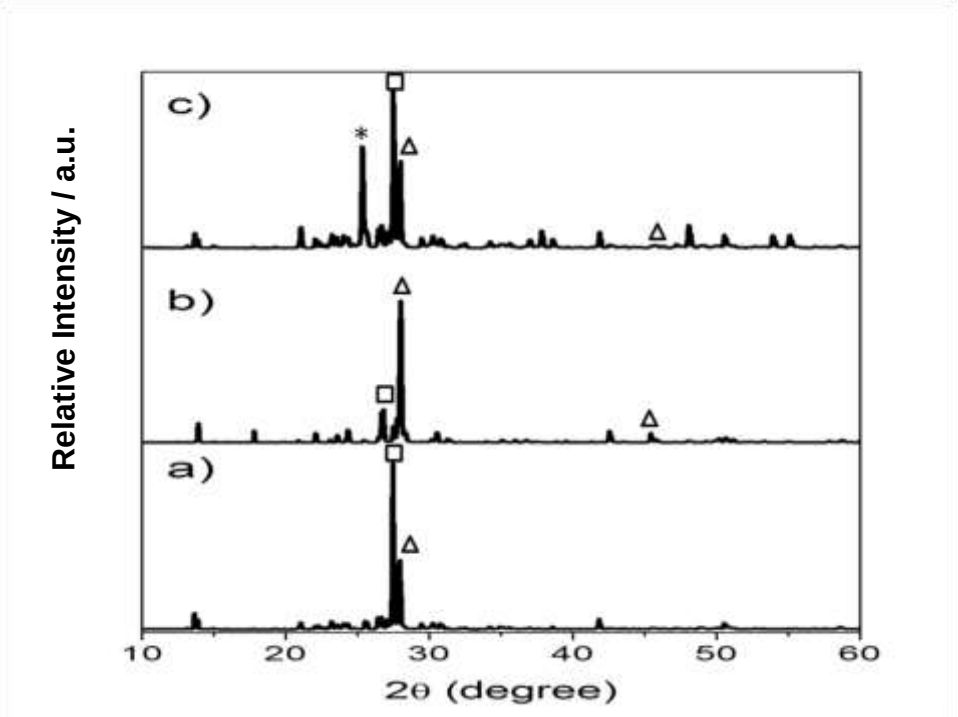

Figure 4.

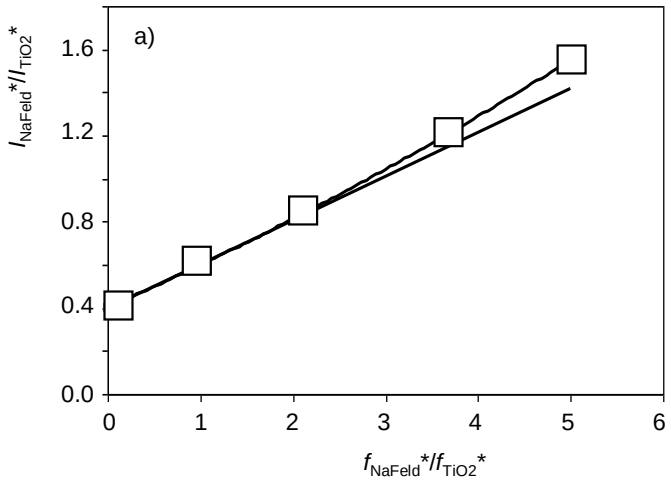
a)
1.6
1.2
0.8
0.4
0.0
0
1
2
3
4
5
6
$I_{NaFeld}*/I_{TiO2}*$
$f_{NaFeld}*/f_{TiO2}*$

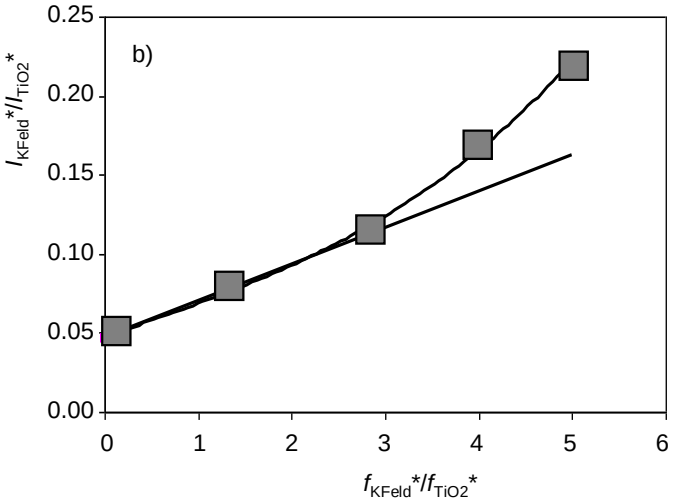
b)
0.25
0.20
0.15
0.10
0.05
0.00
0
1
2
3
4
5
6
$I_{KFeld}*/I_{TiO2}*$
$f_{KFeld}*/f_{TiO2}*$

Figure 5.

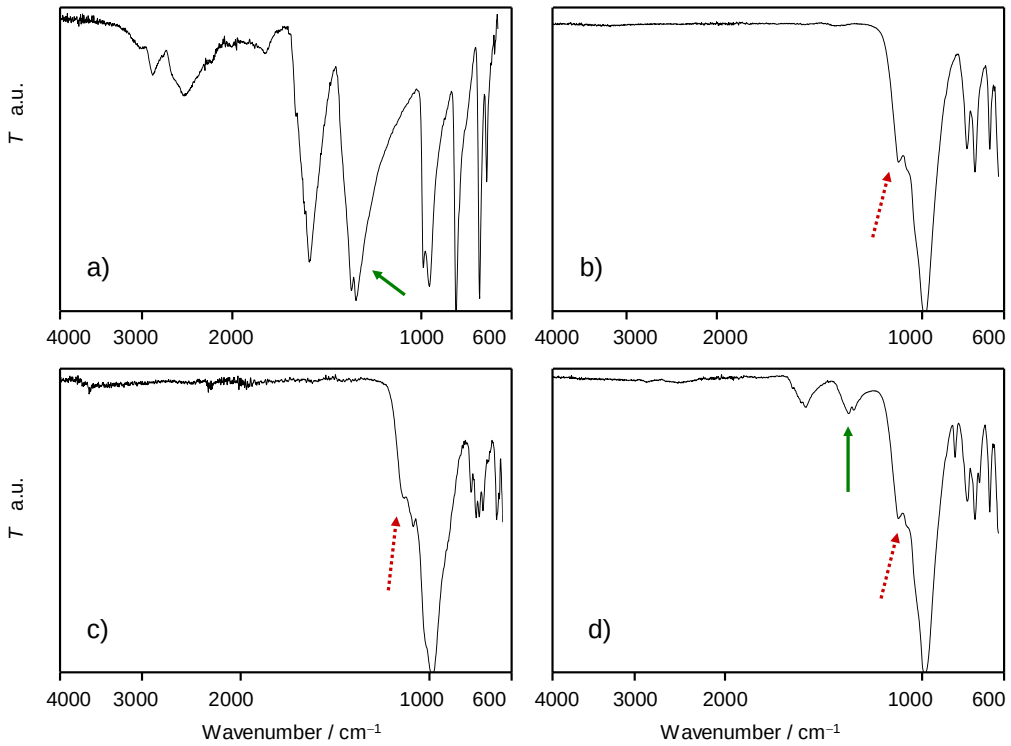

Figure 6.

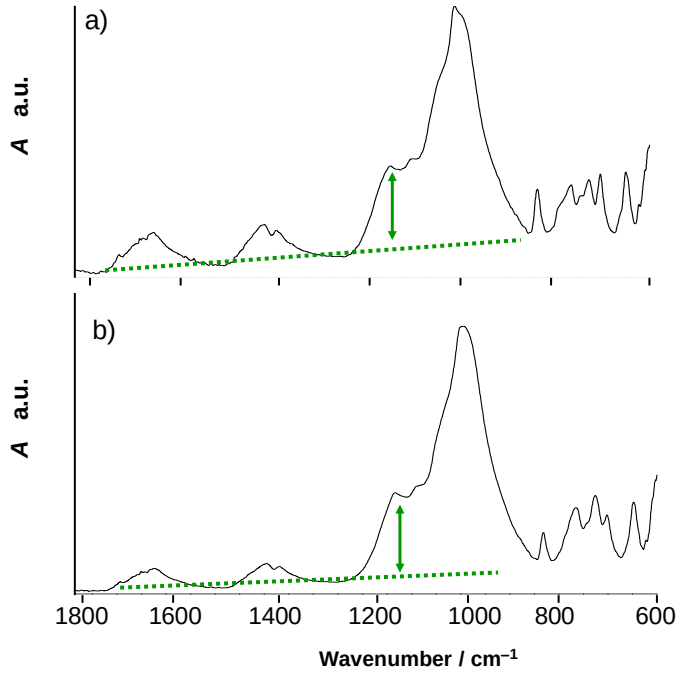

Figure 7.

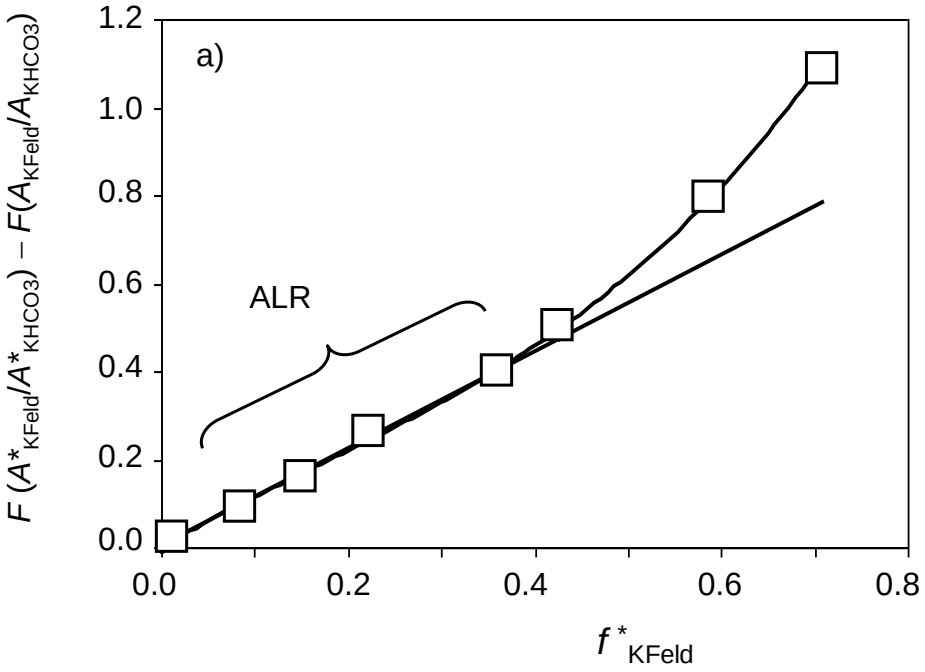
a)
ALR
1.2
1.0
0.8
0.6
0.4
0.2
0.0
0.0
0.2
0.4
0.6
0.8
$F\ (A^*_{KFeld}/A^*_{KHCO3}) - F(A_{KFeld}/A_{KHCO3})$
f^*_{KFeld}

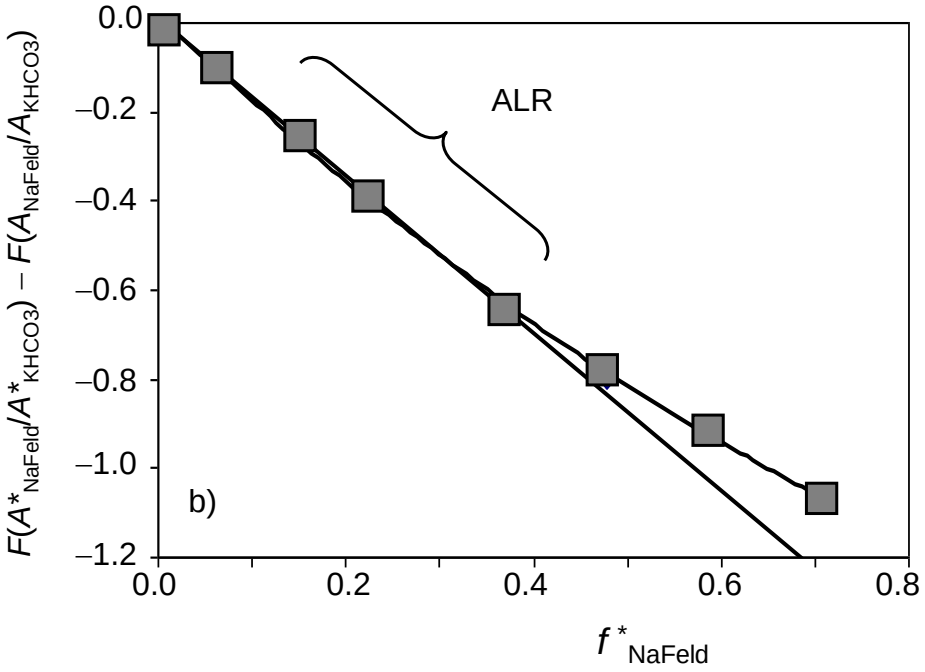
b)
ALR
0.0
–0.2
–0.4
–0.6
–0.8
–1.0
–1.2
0.0
0.2
0.4
0.6
0.8
$F(A^*_{NaFeld}/A^*_{KHCO3}) - F(A_{NaFeld}/A_{KHCO3})$
f^*_{NaFeld}

Supplementary information

Figure S.1. Theoretical the I^*_Y/I^*_P vs. f^*_Y/f_P representations according to Eq. (10), taking I_Y/I_P = 1; I^o_Y/I^o_P = 1, f_Y = 0.10, and f_P = 0.10. a) b^*_Y =1, b^*_P=1; b) b^*_Y =0.5, b^*_P=5; c) b^*_Y =10, b^*_P=20; d) b^*_Y =10, b^*_P=11; e) b^*_Y =1, b^*_P=20.

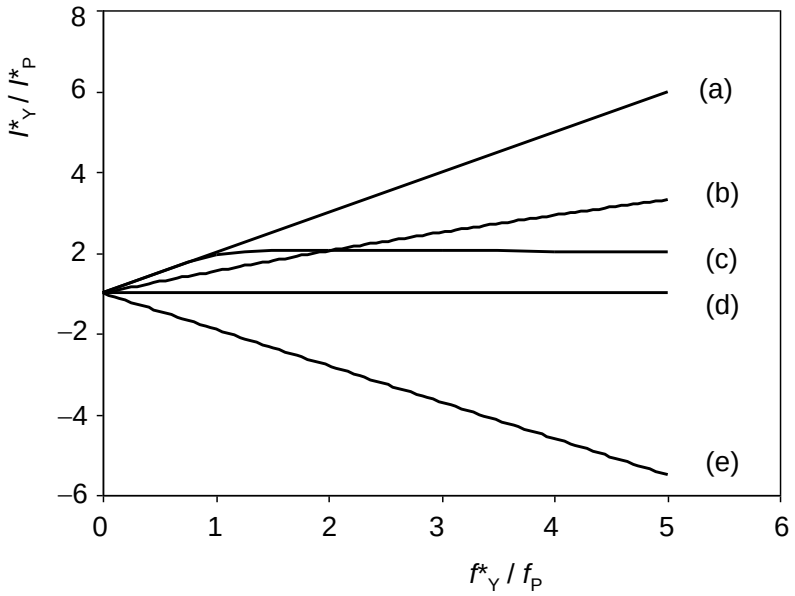

Figure S.2 depicts the diffractograms corresponding to mixed specimens all containing a mass fraction of TiO_2 of 0.100±0.002, and mass fractions of: a) 0.100±0.002 of SiO_2, and 0.800±0.002 of MgO, b) 0.400±0.002 of SiO_2, and 0.500±0.002 of MgO. Figure 5 shows the representation of I^*_{SiO2}/I^*_{TiO2} vs. f^*_{SiO2}/f_{TiO2} corresponding to standard additions graphs obtained by measuring the intensity of peaks at 2Θ = 25.3 and 27.4 degrees for TiO_2 and SiO_2, respectively taking as a problem sample a mixture containing a mass fraction of SiO_2 of 0.100±0.002 and a mass fraction of MgO of 0.800±0.002. Here, the standard addition experiments were performed using TiO_2 internal standard with a mass fraction of 0.100±0.002. Here, the linear fit of the three first data points I^*_{SiO2}/I^*_{TiO2} = (1.52±0.03)(f^*_{SiO2}/f_{TiO2}) + 1.52±0.04 (N = 3; r = 9998), resulting in a value of f_{TiO2} in the problem sample of 0.100±0.005, in close agreement with the expected value of 0.100.

Experimental data fit well, in all the studied cases, to a 2nd order polynomic variation of I^*_Y/I^*_P on f^*_Y/f_P. For data in Figure 6, I^*_{SiO2}/I^*_{TiO2}= 1.488 + 1.799 f^*_{SiO2}/f_{TiO2}− 0.114 $\left(f^*_{SiO2}/f_{TiO2}\right)^2$ (r = 0.9990), while for data in Figure 3a, I^*_{NiO}/I^*_{TiO2}= 0.195 + 0.203 f^*_{NiO}/f_{TiO2}− 0.0203 $\left(f^*_{NiO}/f_{TiO2}\right)^2$ (r = 0.9998) and I^*_{Cr2O3}/I^*_{TiO2}= 0.398 + 0.405 f^*_{Cr2O3}/f_{TiO2} (r = 0.997).

Figure S.2. X-ray diffractograms of samples containing a mass fraction of TiO_2 of 0.100±0.002, and mass fractions of: a) 0.100±0.002 of SiO_2, and 0.800±0.002 of MgO, b) 0.400±0.002 of SiO_2, and 0.500±0.002 of MgO. Peak intensity measurements at 2Θ = 25.3, 27.4, and 20.9 degrees for TiO_2, SiO_2, and MgO, respectively. (* TiO_2, $^{\Delta}$ MgO and $^{\square}$ SiO_2)

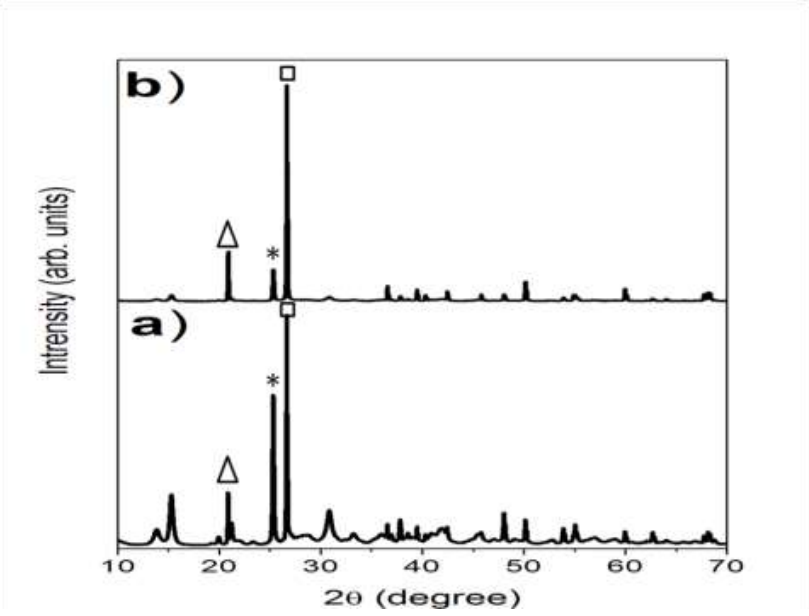

Figure S.3. Plots of I^*_{SiO2}/I^*_{TiO2} vs. f^*_{SiO2}/f_{TiO2} from XRD data in standard additions experiments using TiO_2 as the internal standard.

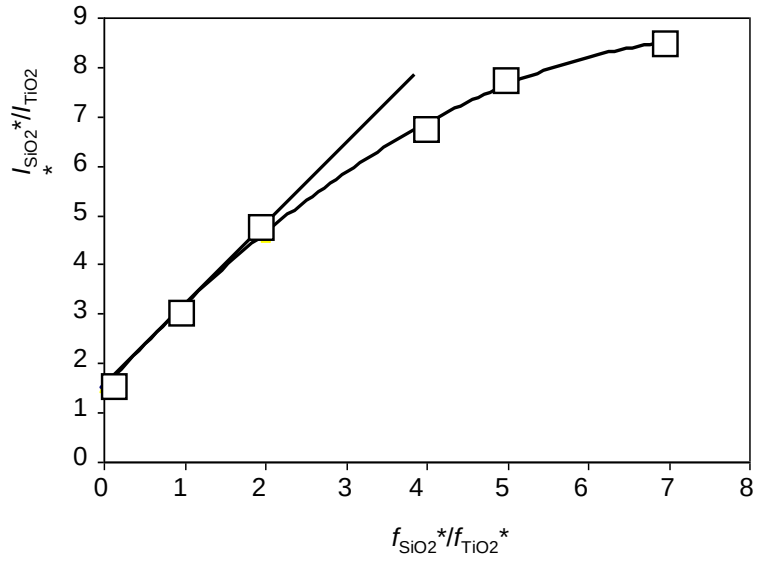

Figure S.4. The variation of the relative uncertainty in the concentration ratio, $\Delta(f_Y/f_P)/(f_Y/f_P)$, on the mass fraction ratio ζ for ξ = 1.0 assuming $\Delta f/f_\circ$ = 1% and taking different values of the $\Delta I/I_\circ$ ratio.